Ab initio phase stabilities of Ce-based hard magnetic materials and comparison with experimental phase diagrams

Halil İbrahim Sözen,[1] Semih Ener,[2] Fernando Maccari,[2] Konstantin P. Skokov,[2] Oliver Gutfleisch,[2] Fritz Körmann,[1] Jörg Neugebauer,[1] and Tilmann Hickel[1]

[1]*Max-Planck-Institut für Eisenforschung GmbH, Max-Planck-Str. 1, 40237 Düsseldorf, Germany*

[2]*Functional Materials, Department of Material Science Technische Universität Darmstadt, 64287, Darmstadt, Germany*

(Received 22 February 2019; published 12 August 2019)

Recent developments in electrical transportation and renewable energies have significantly increased the demand of hard magnetic materials with a reduced critical rare-earth content, but with properties comparable to (Nd,Dy)-Fe-B permanent magnets. Though promising alternative compositions have been identified in high-throughput screenings, the thermodynamic stability of these phases against decomposition into structures with much less favorable magnetic properties is often unclear. In the case of Ce-Fe-Ti alloys, we have used finite temperature *ab initio* methods to provide this missing information. Employing state-of-the-art approaches for vibrational, electronic, and magnetic entropy contributions, the Helmholtz free energy, $F(T, V)$, is calculated for the desired hard magnetic $CeFe_{11}Ti$ phase and all relevant competing phases. The latter have been confirmed experimentally by employing reactive crucible melting (RCM) and energy-dispersive x-ray spectroscopy (EDS). Our *ab initio* based free energy calculations reveal that the presence of the $CeFe_2$ Laves phase suppresses the formation of $CeFe_{11}Ti$ up to 700 K. The result is in agreement with RCM, in which $CeFe_{11}Ti$ is only observed above 1000 K, while the $CeFe_2$ and Ce_2Fe_{17} phases are stable at lower temperatures.

DOI: 10.1103/PhysRevMaterials.3.084407

I. INTRODUCTION

Most of the currently applied hard magnetic materials are alloys that are composed of rare-earth (RE) and transition metal (TM) elements. In the last decades, such alloys have received a lot of scientific and technological attention due to rapid developments in industrial applications connected to electrical transportation and renewable energies [1]. Hard magnetic materials crucially affect the functionality, sustainability, and performance of devices such as electrical engines in cars or generators in wind turbines. A high magnetic energy density is desired for these materials, which has most convincingly been achieved with the discovery of $Nd_2Fe_{14}B$ magnets in 1984 [2,3].

However, conventional Nd-Fe-B magnets have limited sustainability at elevated operation temperatures, due to the degradation of coercivity. Furthermore, to achieve higher anisotropy fields [4] and Curie temperatures (T_C), Dy is added to these alloys [5]. This heavy RE element is often considered to be one of the most critical elements for future applications, with Nd not far behind on the list [6,7]. In addition, given the increasing demand in combination with high prices, there are considerable efforts to design new and alternative RE-lean and RE-free hard magnetic materials [8,9].

In this extent, the exploration of Ce-based hard magnetic materials is promising: First, Ce is, in contrast to Dy and Nd, a rather abundant and easily accessible rare-earth element [10], which makes it comparatively inexpensive [11]. Second, depending on the valency, the magnetic anisotropy, originating from the Ce $4f$ electrons, can in principle be even stronger than for Dy or Tb [12]. It turns out that in actual materials such as $Ce_2Fe_{14}B$, the Ce $4f$ electrons occupy higher energy conduction bands and make Ce tetravalent. The application of mechanical or chemical pressure may result in trivalent states, because the Ce valence states show a high steric volume dependence [13,14]. The latter valency is attractive since it has a higher magnetic anisotropy.

The main challenge for Ce-based magnetic materials is the formation of a secondary $CeFe_2$ phase. This phase forms in the microstructure [15], retards the crystallization of ternary hard magnetic phases and obstructs the formation of RE-rich paramagnetic phases that crucially diminish coercivity of these alloys and compounds [16–18]. The physical properties of this phase have been investigated previously [16,18–24]. However, the conditions under which this detrimental phase emerges and why it hinders the formation of hard magnetic phases are currently not understood. In order to produce sustainable and reliable hard magnetic materials, a scheme to predict the relative phase stabilities of all involved phases is therefore required.

In the present work, we report *ab initio* based temperature dependent phase formation diagrams for Ce-TM-X (X = W, Ti, Mo, Si, or Al) hard magnetic materials. We select Ce-Fe-Ti as a prototype system to test our approach since a few experimental studies on this system are available. Going beyond the previously published experimental data, we performed reactive crucible melting (RCM) and energy dispersive spectrum (EDS) analysis to complement and benchmark the theoretical insights.

The paper is organized as follows. In Sec. II, we explain the technical aspects of our computational and experimental methods. In Sec. III, the relevant phases for the determination of a Ce-Fe-Ti phase formation diagram are identified. In

Sec. IV, RCM and EDS results of Ce-Fe-Ti and relative phase stabilities of competing phases are discussed. We finally conclude the paper with remarks and discussions in Sec. V.

II. COMPUTATIONAL AND EXPERIMENTAL DETAILS

A. Computational methodology

We use density functional theory (DFT) as implemented in the Vienna *ab initio* simulation package VASP [25]. The projector-augmented wave (PAW) [26] method is employed. In particular, the Ce potential with $5s^2 5p^6 4f^1 5d^1 6s^2$ valence configuration is selected, where the single f electron is treated explicitly as valence state. Exchange correlation is treated within the generalized gradient approximation (GGA) of Perdew, Burke, and Ernzerhof (PBE) [27].

The unary element Ce is known to exist in four allatropic phases at atmospheric pressure [28], of which γ and α-Ce receive most of the scientific attention. The high-temperature/volume phase γ-Ce exhibits local magnetic moments with a Curie-Weiss behavior of the susceptibility in the Ce^{3+} configuration. In the low-temperature/volume phase α-Ce, the f electrons are more delocalized (bandlike) and exhibit a typical Pauli paramagnetism in the Ce^{4+} configuration. Ce^{3+} has a single $4f$ electron, which is subjected to strong localization effects. Available DFT exchange-correlation functionals have difficulties to accurately capture the properties of strongly localized electrons. Specifically, they often give rise to an unphysical delocalization, which causes a severe self-interaction contribution. The fact that some fractions of the charge density attract and repel each other further causes a delocalization of the wave functions. In order to overcome this challenge and to correctly reproduce the α-γ isostructural phase transformation, we go for pure Ce beyond conventional DFT and use as a correction scheme the DFT + U approach [29]. However, the DFT + U approach is only required for the treatment of unary γ-Ce. In the case of Ce-based binaries as well as the Ce-Fe-Ti ternary investigated here, no Hubbard U correction is applied. The underlying reason for this is the strong hybridization of Ce-$4f$ with TM-$3d$ electrons, which gives rise to an earlier filling of the bonding bands compared to the localized $4f$ of Ce.

In order to calculate phase stabilities and thermodynamic properties, DFT is not only applied to ground-state energies, but also to finite temperature excitations [30]. The free energies are considered in the adiabatic approximation, therewith decoupling the degrees of freedom

$$F(T,V) = E_0(V) + F^{\mathrm{el}}(T,V) + F^{\mathrm{vib}}(T,V) + F^{\mathrm{mag}}(T,V), \tag{1}$$

which are the zero-temperature total energy E_0, electronic F^{el}, vibrational F^{vib}, and magnetic F^{mag} contributions of the free energy.

The electronic contribution to the free energy F^{el} is calculated by using the finite temperature formulation of DFT [31]

$$F^{\mathrm{el}} = E^{\mathrm{tot}}(T,V) - E_0(V) - TS^{\mathrm{el}}, \tag{2}$$

where E^{tot} is the total electronic free energy (including the binding energies at 0 K). S^{el} is the electronic entropy obtained from Fermi occupation numbers f_i,

$$S^{\mathrm{el}} = 2k_{\mathrm{B}} \sum_i (f_i \ln f_i + (1-f_i)\ln(1-f_i)), \tag{3}$$

with k_{B} the Boltzmann constant. We note that the electronic contribution is evaluated for static lattice positions, though lattice vibrations and anharmonic effects modify the electronic density of states and electronic entropy close to the melting point [32]. The evaluation of these coupling effects requires explicit *ab initio* molecular dynamics simulations, which is beyond the scope of the present manuscript.

Phonon spectra are computed with the *direct force constant method* [33,34] and used as an input for the vibrational free energy F^{vib} as well. This approach is based on the calculation of Hellmann-Feynman forces for supercells containing small atomic displacements (such as ∼0.02 Å). The eigenvalues of the Fourier transformed dynamical matrix ω_i enter the free energy expression in harmonic approximation [35]:

$$F^{\mathrm{vib}} = \frac{1}{N} \sum_i^{3N} \left\{ \hbar\omega_i + k_{\mathrm{B}} T \ln\left[1 - \exp\left(-\frac{\hbar\omega_i}{k_{\mathrm{B}} T} \right) \right] \right\}, \tag{4}$$

where $\hbar$ is the reduced Planck constant. The summation in Eq. (4) runs over all $3N$ phonon states, where N is the number of atoms in the unit cell. In the *quasiharmonic approximation* considered here, the volume dependence of the phonon frequencies ω_i is additionally taken into account. Explicitly anharmonic contributions are not considered. We note that in many magnetic materials, the phonon frequencies may depend on the actual magnetic state (see e.g., Refs. [36,37]). Due to its computational expenses we do not include this coupling into the present work and leave it for future investigations.

The magnetic free energy F^{mag} is treated with an empirical formula developed by Inden [38,39]. It requires as input parameters the Curie temperature, the mean magnetic moment and the magnetic enthalpy ratio of short- to long-range order. Chen and Sundman [40] modified the model to handle the phase transformation between the bcc and fcc phases of pure Fe. In another refinement, Xiong *et al.* [41] consider an effective magnetic moment rather than the mean magnetic moment, in order to take antiferromagnetic interactions into account. According to his work, the magnetic free energy as function of relative temperature $\tau = T/T_C$ is given as

$$F^{\mathrm{mag}} = TS^{\mathrm{mag}} g(\tau), \tag{5}$$

$$g(\tau) = \begin{cases} 0 & \tau \leqslant 0 \\ 1 - \frac{1}{D}\left[0.38438376\frac{\tau^{-1}}{f} + 0.63570895\left(\frac{1}{f} - 1\right)\left(\frac{\tau^3}{6} + \frac{\tau^9}{135} + \frac{\tau^{15}}{600} + \frac{\tau^{21}}{1617}\right)\right] & 0 < \tau \leqslant 1, \\ -\frac{1}{D}\left(\frac{\tau^{-7}}{21} + \frac{\tau^{-21}}{630} + \frac{\tau^{-35}}{2975} + \frac{\tau^{-49}}{8232}\right) & \tau > 1 \end{cases} \tag{6}$$

$$D = 0.33471979 + 0.49649686\left(\frac{1}{p} - 1\right). \quad (7)$$

Here, p is an optimized structural factor, which is 0.37 for bcc and 0.25 for non-bcc crystal structures. Since the notion of effective magnetic moments is most suitable for the material systems discussed in this work, we employ this approach. In this context, the magnetic entropy in the high-temperature limit, $S_{\max}^{\mathrm{mag}}$, is written as

$$S_{\max}^{\mathrm{mag}} = k_{\mathrm{B}} \sum_i x_i \ln(\beta_i + 1). \quad (8)$$

x is the composition of magnetic sublattice per formula unit and β is the local magnetic moment. Further details can be found in Ref. [41]. We note that a similar approach has been employed recently to investigate the partitioning of substitutional impurities in cementite and ferrite [42].

B. Experimental method

Our work is complemented by experimental investigations on samples, which have been synthesised with reactive crucible melting (RCM). The details of this method are described elsewhere [43–46]. The iron crucibles were fabricated from commercial purity (99, 99 + %) iron rods and other elements were added as in powder form (Ti 99.5%, Ce 99.9%). The powder filled crucibles were sealed under inert Ar gas atmosphere and wrapped in steel foils, then sealed in an evacuated quartz tube and subsequently annealed. Filling ratios between Ce and Ti are selected to be 1:1 as previous investigations show no significant difference for 2:1 and 1:2 filling ratios (not shown here). Sealed crucibles were heated up to the desired temperatures and kept there for 24 h. The samples were quenched in water to ensure rapid cooling.

After the RCM process, the resulting crucibles were cut into halves and the surfaces were polished. Microstructural characterization and chemical composition analysis were done on these polished surfaces. Chemical compositions of the phases were determined with a TESCAN scanning electron microscopy (SEM) in backscattered electron (BSE) contrast using energy dispersive x-ray (EDS) analysis. To avoid statistical errors the EDS analysis was done at different parts of the crucible at different points. The outcome of the SEM-EDS analysis are plotted in ternary diagrams to display the chemical composition variation for each possible phase in the Ce-Fe-Ti system.

III. RELEVANT PHASES IN THE CE-FE-TI SYSTEM

The final goal of this work is the derivation of temperature-composition phase diagrams in order to address properties like the synthesizability or the long-term sustainability of promising hard-magnetic phases. There are currently no reliable phase diagrams for this ternary system available in the literature. A decisive contribution to the construction of phase diagrams is the calculation of the temperature dependent formation energies of all relevant phases. The latter can be complex binary and ternary compounds as listed for instance in Pearson's Crystal Data [47].

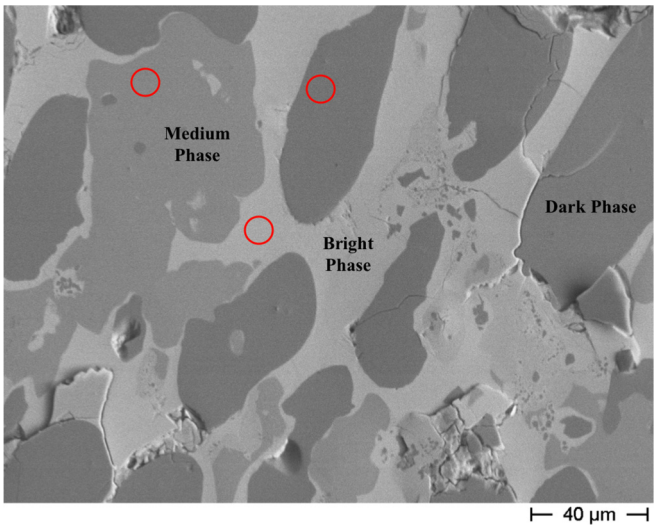

FIG. 1. BSE image of $Ce_{15}Fe_{71}Ti_{14}$ sample by SEM. Red circles indicate the position of EDS spot analysis.

Already for a single alloy, experimental investigations indicate the presence of a variety of phases. In Fig. 1, the scanning electron microscopy (SEM) image of a sample with nominal composition $Ce_{15}Fe_{71}Ti_{14}$ is given that has been prepared by arc melting technique in argon atmosphere and annealed at 1273 K for 5 days. It shows at least three different phases, which have a different morphology, but are distributed all over the microstructure. For representative spots, indicated by red circles electron diffraction spectroscopy (EDS) has been performed to determine the chemical composition. The EDS microanalysis has been repeated for different spot positions in various phases, resulting into deviations in an acceptable range of ∼0.5 at.%. The corresponding concentrations in Table I indicate that only one of the phases (labeled "medium") has a chemical composition that is within tolarence of ∼1 at.% close to $CeFe_{11}Ti$ (= $Ce_{7.7}Fe_{84.6}Ti_{7.7}$). In addition to this a Ce-rich ("bright") phase, a Fe-rich ("dark") phase is present in the microstructure.

Possible candidates for binary and ternary phases are provided in the Gibbs triangle representation given in Fig. 2. An important step to evaluate their relevance for phase stabilities in actual materials, is the calculation of their formation energy. A prerequisite is, however, reliable and high-quality references. Therefore we carefully computed the energetic and magnetic properties of all phases in the Ce-Fe-Ti system indicated in Fig. 2.

TABLE I. Composition of the spots for different phases are listed in the BSE image in Fig. 1 (at. %).

Spot position	Ce	Fe	Ti	Corresponding phase
Bright phase	35.16	63.82	1.02	$Ce(Fe, Ti)_2$
Medium phase	8.61	83.57	7.82	$Ce(Fe, Ti)_{12}$
Dark phase	1.06	69.44	29.50	$(Fe, Ce)_2Ti$

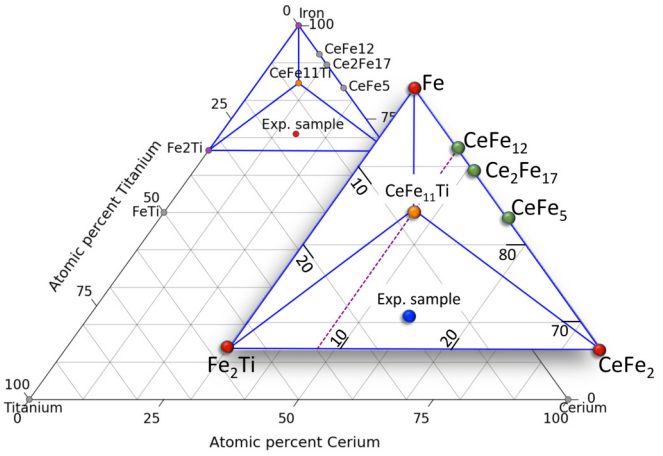

FIG. 2. Gibbs diagram of relevant phases in the Ce-Fe-Ti system. The zoom focuses on the Fe-rich corner of the diagram, which contains the technologically relevant phase $CeFe_{11}Ti$.

A. The unaries Ce, Fe, and Ti

Geometric, elastic, and magnetic parameters of the unaries, as we determine them by DFT, are given in Table II. The excellent agreement with the experimental reference data provides confidence in the predictive power of our DFT approach. Note that the trend of PBE observed for many metals to overestimate the lattice constant and to underestimate the bulk modulus [34,55] is not seen for the present elements.

In the case of unary Ce, we paid special attention to the description of the $4f$ character and its impact on formation energies. From a theoretical point of view, the most challenging physical property of Ce, which has already been subject of extensive debates in the literature, is its isostructural α-γ phase transformation. In this work, we treat α-Ce as nonmagnetic (NM) and γ-Ce as ferromagnetic (FM), similarly to what has been assumed in many previous studies [56–60].

As shown in Fig. 3(a), conventional DFT yields at $T = 0$ K only a local minimum for the nonmagnetic α state. Nevertheless, if the volume expands, a FM phase becomes energetically more stable above the experimental lattice constant of γ-Ce. The γ-Ce state can, for example, be further stabilized by magnetic entropy [61]. Within DFT the γ-Ce state additionally gains (meta)stability if a finite Hubbard U is applied to the $4f$ band, as shown in Fig. 3(b). This is required for the phonon calculations discussed below. Experimentally, it is reported that α-Ce is more stable at room temperature by

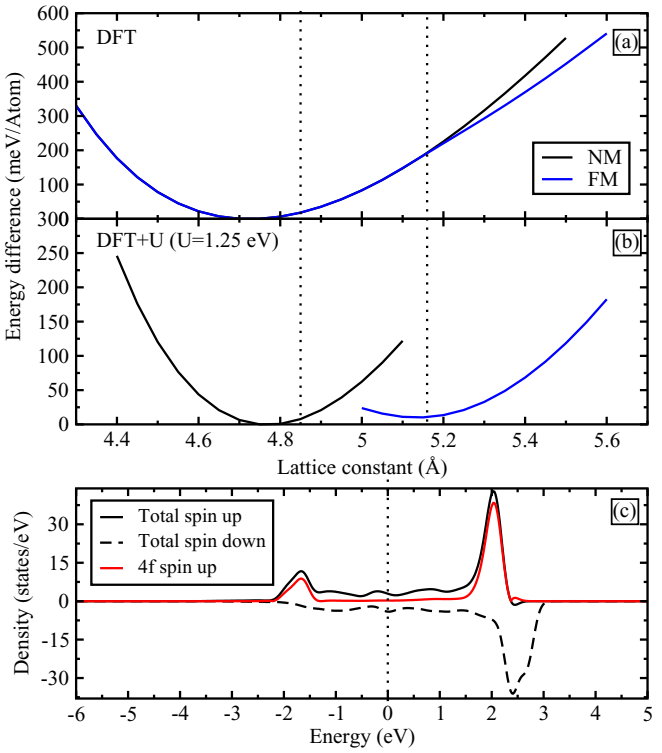

FIG. 3. Ground-state energetics of fcc-Ce with (a) DFT and (b) DFT + U with $U = 1.25$ eV. The dashed vertical lines represent experimental lattice constants that are 4.85 Å for α-Ce and 5.16 Å for γ-Ce. (c) The calculated DOS obtained by DFT + U with $U = 3.5$ eV, where the vertical line indicates the Fermi level.

$\sim$20 meV [61]. This energy difference is well reproduced by the choice $U = 1.25$ eV.

A finite U value can be further motivated by inspecting the electronic band structure. The electronic structure of γ-Ce as measured by x-ray photoemission spectroscopies [62,63] contains a peak below the Fermi energy at $\sim$2 eV. For conventional DFT, this peak is not reproduced, but it can be observed by DFT + U with an U value of $\sim$3.5 eV as shown in Fig. 3(c). This indicates that although a finite U value can in principle improve the conventional DFT results, there seems to be no unique U parameter that simultaneously models all relevant properties. A smaller U value of $\sim$1.25 eV reproduces the correct phase stabilities, whereas a larger U of $\sim$3.5 eV allows for a better agreement of the underlying electronic

TABLE II. Physical properties of the pure elements Ce, Fe, and Ti. a and c are the lattice constants, B_0 and M are the bulk modulus and the magnetic moment.

Element	a (Å)	c (Å)	B_0 (GPa)	M (μ_B)
Ce	4.715	4.715	29	NM
Exp.	4.817 [48]	4.817 [48]	27 [49]	PM [51,52]
	4.85 [48]	4.85	24 [50]	
Fe	2.837	2.837	168	2.21
Exp.	2.868 [53]	2.868 [53]	168 [53]	2.22 [53]
Ti	2.925	4.619	117	NM
Exp.	2.951 [54]	4.684 [54]	106 [54]	NM [54]

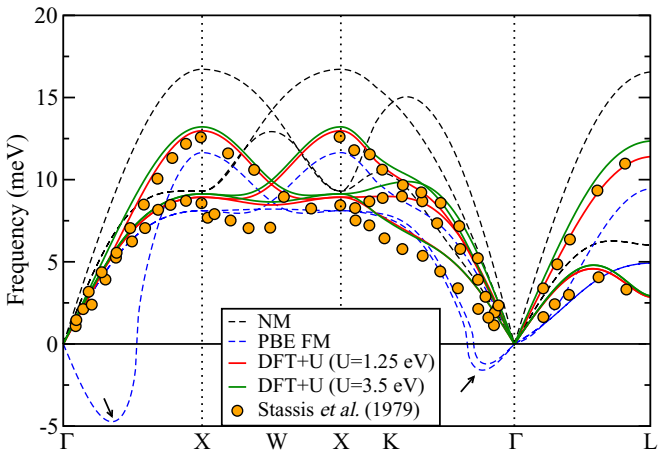

FIG. 4. Calculated phonon dispersion lines for Ce along high-symmetry directions. Dashed black lines represent a NM treatment of Ce with the equilibrium lattice constant $a = 4.715$ Å; blue dashed lines represent a FM treatment of Ce with the constrained lattice constant $a = 5.20$ Å. Solid red and green lines correspond to a DFT + U treatment with a Hubbard U of 1.25 and 3.5 eV, respectively. Orange dots belong to measured data for γ-Ce by Stassis *et al.* [64] with an experimental lattice constant of $a = 5.16$ Å.

structure. A similar finding was made by Tran *et al.* [60], who used full-potential linearized augmented plane waves to solve the Kohn-Sham equations. They also reported a set of two different U parameters (1.5 and 4.3 eV) to correctly mimic the energetics between both phases and the electronic properties.

In order to obtain an accurate and consistent understanding of the phase stabilities, the comparison of calculated thermodynamic properties with experimental data is vital. We therefore compare in Fig. 4 the phonon spectra (determining the vibrational free energy) of γ-Ce with available experimental data [64]. The experiments were performed at room temperature. To the best of our knowledge there are no experimental phonon spectra available for α-Ce. We first observe that a NM treatment fails to reproduce the experiments. One reason for this is that the NM theoretically determined lattice constant is smaller than in experiment, which makes the material stiffer and causes higher frequencies, in particular for the optical phonon branches.

As mentioned above, a FM treatment of γ-Ce is energetically preferred around the experimental lattice constant. We have therefore constrained the lattice constant in the phonon calculations to $a = 5.20$ Å yielding a magnetic moment of $\sim 0.4\ \mu_B$. As long as this configuration does not correspond to a local minimum in the potential energy surface [compare Fig. 3(a)], imaginary frequencies around the high-symmetry Γ point are observed. The impact of a Hubbard U on the phonons has been checked with $U = 1.25$ eV (optimal value for the energetics) as well as for $U = 3.5$ eV (optimal value with respect to spectroscopic properties). We find that their overall behavior is very similar. We relate this to the same employed lattice constants ($a = 5.161$ Å) and to the fact that the vibrations mostly depend on the crystal structure and lattice parameters rather than the electronic structure.

B. Fe-Ti binary alloys

The binary phase diagram of the Fe-Ti system [65] contains only binary stable phases for two compositions: FeTi and Fe_2Ti. The intermetallic FeTi compound has the CsCl structure and is nonmagnetic. The second stoichiometric compound Fe_2Ti has the $MgZn_2$ type Laves structure, designated C14. There are two distinct Fe symmetry sites in Fe_2Ti, namely, Fe($2a$) and Fe($6h$). At 4 K, the magnetic moments of Fe($6h$) in the same layer are ferromagnetically aligned, whereas the magnetic coupling between adjacent layers is antiferromagnetic. The resulting magnetic moment at the Fe($2a$) site is zero. This is likely a result of magnetic frustration as these Fe-sites are situated between two antiferromagnetic layers [66]. Some of the calculated physical and magnetic properties are shown in Table III.

A first evaluation of phase stabilities can be performed by comparing the formation energies at $T = 0$ K. The formation energies of the known Fe-Ti alloys are calculated with respect to the pure metallic unary phases of α-Fe and α-Ti. Our theoretical calculations predict the formation energies to be -0.419 and -0.283 eV/atom for FeTi and Fe_2Ti, respectively. As shown in Fig. 5, FeTi is the compound with the lowest formation energy. In addition, Fe_2Ti is also slightly below the common tangent line that indicates this compound already forms at $T = 0$ K above 66.6% content of Fe. This could explain the presence of a ("dark") phase with similar composition in our SEM micrograph in Fig. 1, though the sample was heat treated at higher temperatures.

In order to obtain finite temperature phase stabilities, we have also computed the phonon dispersions at the theoretical (i.e., relaxed) and experimental lattice constant of FeTi, shown

TABLE III. Physical properties of stable Fe-Ti compounds. The symbols are chosen as in Table II.

Alloy	a (Å)	c (Å)	B_0 (GPa)	M (μ_B)
FeTi	2.948	2.948	197	NM
Exp.	2.977 [67]	2.977 [67]	189 [67]	NM [70]
	2.975 [68]	2.975 [68]	160.8 [69]	
Fe_2Ti	4.689	7.788	188	1.31 Fe($6h$)
				0 Fe($2a$)
				0.14 Ti($4f$)
Exp.	4.769–4.804 [65]	7.745–7.849 [65]	201 [71][a]	1.4 [66][b]

[a]Value belongs to a theoretical work.

[b]Value corresponds to the average magnetic moment at the $6h$ site, measured at 4 K.

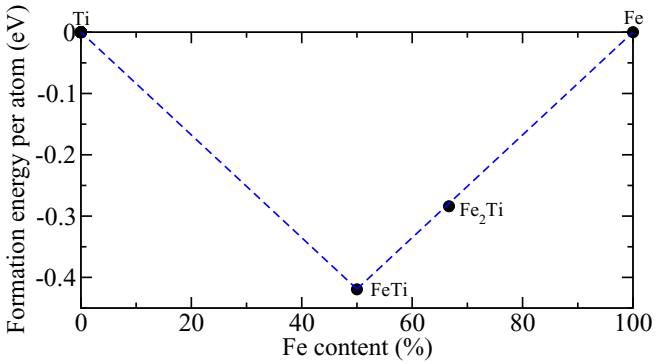

FIG. 5. Calculated formation energies of the two Fe-Ti binaries as a function of Fe content at $T = 0$ K.

in Fig. 6. We further compare our results with experimental phonon dispersions that were determined at room temperature by inelastic neutron scattering experiments [67] in combination with a Born-von-Kármán model employing fitted force constants. The experimental lattice constant, measured at room temperature, is 2.977 Å, whereas our theoretical one is 2.948 Å at $T = 0$ K.

In practice, our calculations have been performed for a $2 \times 2 \times 2$ (16 atoms) and a $3 \times 3 \times 3$ (32 atoms) supercell to study size effects. The difference between the phonon spectra at the experimental and the theoretical lattice constant is found to be small. We further observe that the acoustic branches are in good agreement with the fitted data, whereas there are some minor differences in the optical branches. The good description of the low-energy region is most important for the derived free energies, where we also observe a reasonable convergence with respect to supercell size.

An important quantity for an evaluation of our full thermodynamic approach [see Eq. (1)] is the heat capacity, since it sensitively depends on the total free energy and can be directly compared to experiment. In this case, the relevance of supercell effects mentioned above can be evaluated more systematically. As seen in Fig. 7, a $1 \times 1 \times 1$ (2 atoms) cell is

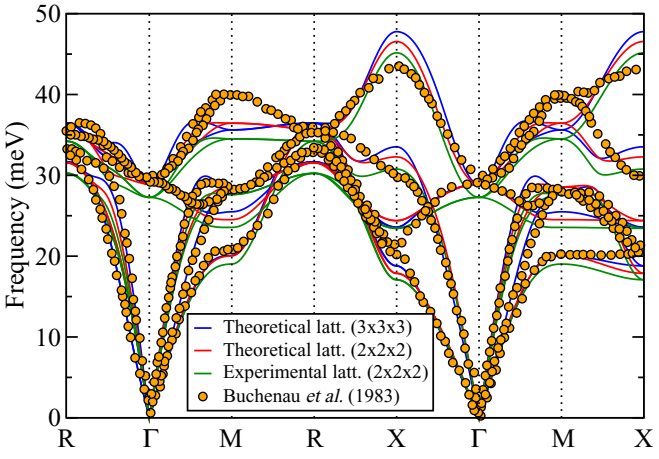

FIG. 6. Calculated phonon dispersion relation of B2-FeTi compared to neutron scattering experiments performed at room temperature.

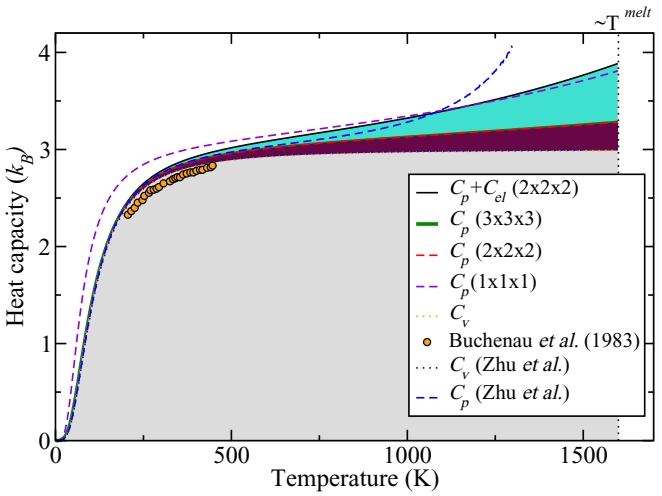

FIG. 7. Calculated heat capacity for B2-FeTi as compared to both experiment [65] and theoretical work performed by Zhu *et al.* [72]. The dotted vertical line indicates the melting temperature 1590 K.

clearly insufficient, while the $2 \times 2 \times 2$ and $3 \times 3 \times 3$ results are almost identical and are therefore considered to be converged. The agreement of our isochoric heat capacity C_v with experimental data (available from ~200–450 K) is good. Employing the quasiharmonic approximation, we also calculate the isobaric heat capacity C_p and the electronic contribution C_{el}. Only C_v is, however, experimentally available [67]. We also compared our results with another theoretical approach reported by Zhu *et al.* [72], where the dynamical matrix has been approximated using a combination of elastic constants and structural parameters. In contrast to their work, the direct force constant method employed in the present paper does not yield a divergence close to the melting temperature.

C. Fe-Ce binary alloys

X-ray diffraction and metallography analysis indicate the existence of only two binary Fe-Ce compounds, which are Ce_2Fe_{17} and $CeFe_2$ [73–75]. There are some reports in the literature [73] about the synthesis of $CeFe_5$, which seems to be a fictitious compound with $CaCu_5$ structure. If every third Ce atom in $CeFe_5$ is replaced by a pair of Fe atoms ($CeFe_5$ = Ce_3Fe_{15} → $Ce_2Fe_2Fe_{15}$), the composition Ce_2Fe_{17} is obtained. Although its presence has not been confirmed in subsequent works, we included this phase in our calculations. We further considered the $CeFe_{12}$ phase as an end-member of $CeFe_{11}Ti$. The calculated physical and magnetic properties are shown in Table IV and compared to experimental results from literature.

As stated above, the electronic structures of pure Ce and its compounds are still controversial. We realized that calculations of Ce-Fe alloys do not require any Hubbard U parameter due to the strong hybridization of Fe-3d and Ce-4f electrons. We therefore used conventional DFT for all ground-state calculations, including the pure Ce reference.

Based on the ground-state references, we show in Fig. 8 the formation energies of the considered phases. $CeFe_{12}$ and Ce_2Fe_{17} have slightly positive formation energies with 0.01

TABLE IV. Physical properties of stable Fe-Ce compounds. The symbols are chosen as in Table II.

Alloy	a (Å)	c (Å)	B_0 (GPa)	M (μ_B)
$CeFe_2$	7.218	7.218	91	1.81 Fe($16a$), −0.91 Ce($8b$)
Exp.	7.304 [73]	7.304 [73]	97 [76]	1.29 [73][a] 1.65 Fe($16a$) [77][b], −0.68 Ce($8b$) [77][b]
$CeFe_5$	4.987	4.063	108	2.20 Fe($2c$), 2.18 Fe($3g$), −0.66 Ce($1a$)
Exp.	4.900 [78]	4.136 [78]	-	-
$CeFe_{12}$	8.505	4.652	131	2.49 Fe($8i$), 1.84 Fe($8f$), 2.29 Fe($8j$), −0.81 Ce($6c$)
Exp.	8.504 [79][b]	4.648 [79][b]	-	1.91[80][b]
Ce_2Fe_{17}	8.403	12.641	105	2.59 Fe($6c$), 2.06 Fe($9d$), 2.39 Fe($18f$), 2.23 Fe($18h$), −0.81 Ce($6c$)
Exp.	8.490 [73]	12.416 [73]	-	1.8 [73,81][c]

[a]Value belongs to formula unit (f.u.) due to the absence of neutron diffraction experiment there is no measured decomposition.
[b]Value belongs to a theoretical work.
[c]Value corresponds to the average magnetic moment in Fe sublattice.

and 0.011 eV/atom, respectively. The $CeFe_{12}$ phase does not exist, but it can be stabilized by substitution of transition metal elements (such as Ti [82], V [83], Mo [84], Zr [85], and Si [86]). While the magnetic configuration in the ground state of Ce_2Fe_{17} is not fully clear in the literature, our collinear spin-polarized calculations favor a ferrimagnetic state, with Ce spins aligned antiparallel to the Fe spins. Although its presence has not been confirmed in subsequent works, we included this phase in our calculations. Using the $T = 0$ K formation energies implies that alloys with more than 66.6% Fe content would decompose into $CeFe_2$ and pure Fe.

Since $CeFe_2$ is a phase with a composition that is close to one of the phases observed in our SEM micrograph (bright phase in Fig. 1), we pay special attention to it. Figure 9 shows the phonon spectrum of $CeFe_2$. The phonon dispersion has been measured by inelastic neutron scattering at room temperature by Paolasini *et al.* [87]. They have used a Born-von-Kármán model taking into account longitudinal and transverse forces up to the fifth nearest neighbor. Experimental measurements performed on $CeFe_2$ with a lattice constant of 7.307 Å are compared with our calculations performed at the theoretical lattice constant of 7.218 Å. Paolasini *et al.* indicated their difficulties to find suitable force constants that fit the experimental data. Therefore the agreement of the Born-von-Kármán fit (blue dots) to the actual experimental data (orange dots) presents deviations. Indeed, we find an overall better agreement of our calculated phonon dispersion with the actual experimental than with the fitted data. Due to missing experimental data points, the quality of the acoustic branches in $\Gamma \rightarrow K$ direction is difficult to assess. In general, the deviations to experiment occur at lower energies than in the case of Fe-Ti (Fig. 6).

Another finite temperature property of $CeFe_2$, which can be used for comparison with available experimental data is again the heat capacity, shown in Fig. 10. Haldar *et al.* [88] measured the heat capacity between 3–295 K. The Curie temperature of $CeFe_2$ is 228 K, where C_p consequently shows the common sharp lambda shaped peak. Although our calculations are mainly based on GGA, we also performed a number of cross-checks employing the local density approximation (LDA). The calculations reveal that the C_p values for LDA and GGA only differ above the melting temperature

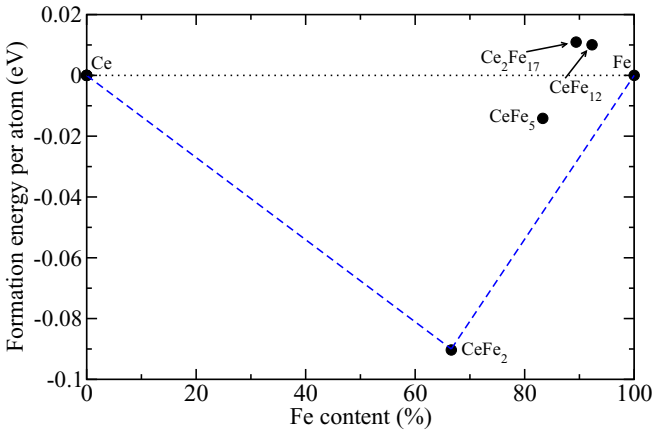

FIG. 8. Calculated formation energies of Fe-Ce alloys as a function of Fe content at $T = 0$ K.

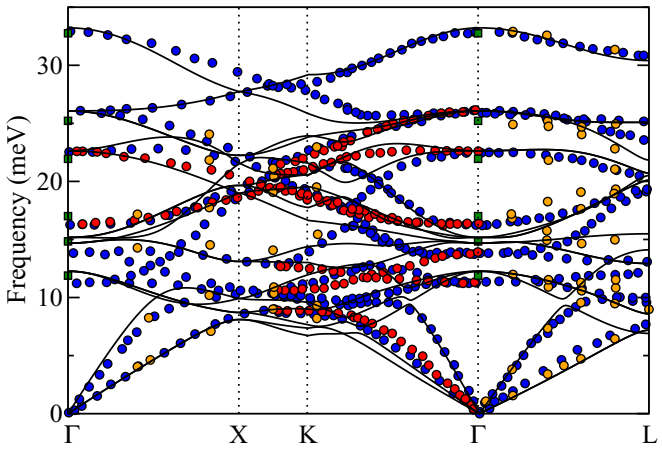

FIG. 9. Calculated phonon dispersion of $CeFe_2$ compared to neutron scattering experiments performed at room temperature [87]. Orange dots are experimental frequencies taken from the longitudinal configuration of the spectrometer. Blue dots are phonon dispersions obtained by fitting data to a Born-von Kármán model. Red dots are branches that are not observable in the scattering plane. Green squares are optical phonon frequencies determined at the centers of the Brillouin zones (Γ point).

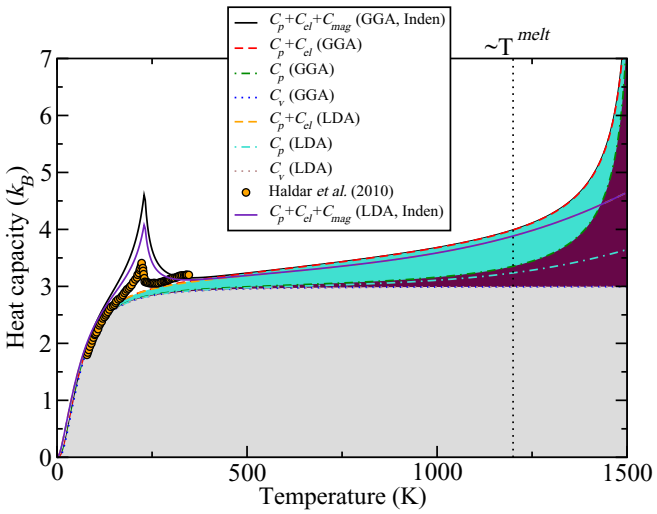

FIG. 10. Calculated heat capacity vs temperature of $CeFe_2$. Various theoretical approaches are compared to experimental data [88]. The vertical line indicates the melting temperature.

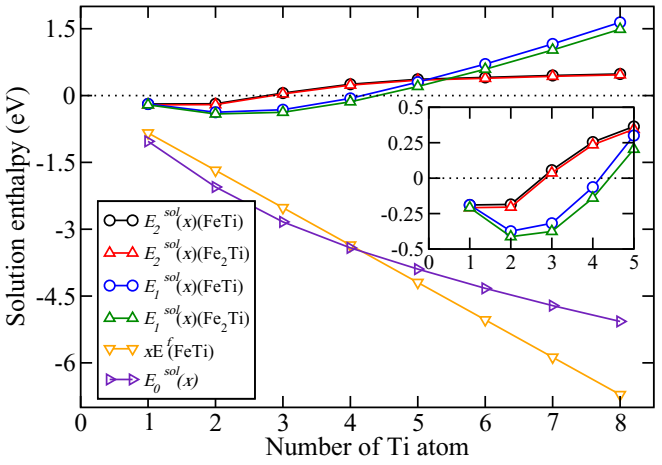

FIG. 11. Calculated Ti solution enthalpies in $CeFe_{12}$ according to Eqs. (11), (12), and (13). The Ti atoms are substituted at 8*i* sites in a $Ce_2Fe_{24-x}Ti_x$ supercell. For each Ti concentration, only the energetically most favorable configuration is considered. For comparison, the formation energy xE^f(FeTi) is plotted as well.

($T_{\rm melt} \sim 1200$ K), while below $T_{\rm melt}$ the differences are nearly negligible. In addition to this, the observed divergence of our GGA data is well above the melting temperature. The vibrational and electronic contributions to C_p are solely determined by DFT. An *ab initio* based calculation of the magnetic contribution is, for example, possible, if a Heisenberg model with exchange integrals obtained by DFT is used [89]. In the present implementation, the empirical model introduced by Inden [90] is used instead. We considered the calculated magnetic moments, as listed in Table IV, the experimental $T_C = 228$ K and the structural parameter $p = 0.37$ as input parameters. Already within this simplified approach a reasonable agreement with experimental data can be achieved. Only close to the peak of the lambda phase transition an overestimation of the heat capacity is observed, which has a small impact on the corresponding free energy.

D. Ce-Fe-Ti ternary alloy

Besides the prototype system of $Nd_2Fe_{14}B$ [80,91], another class of typical compounds that fulfills the technological requirements for hard-magnetic applications is of the form RE-$Fe_{12-x}TM_x$. In case of Ce-Fe alloys, the $CeFe_{12}$ phase does not exist, but alloyed transition metal elements as, for example, a small amount of Ti with $x \geqslant 0.7$, can stabilize this phase [92]. We will therefore derive in the following an approach that will allow us to *ab initio* determine the stabilization energy. Structural parameters of $CeFe_{11}Ti$ are obtained from neutron powder diffraction by Isnard *et al.* [82]. Ce atoms occupy the 2*a* site and Fe atoms are distributed over the three sublattices 8*i*, 8*j*, and 8*f*.

For a theoretical study of the Ti solution in the $CeFe_{12}$ phase, we can expect that there will be no antisites at the Ce 2*a* sites and that the addition of *x* atoms Ti, corresponding to the composition $CeFe_{12-x}Ti_x$, follows the purple dashed line in Fig. 2. We start by substituting a single Ti atom in a 26 (2 f.u.) atom supercell, corresponding to 3.8 at.% Ti, and evaluate different sites, namely, 8*i*, 8*j*, and 8*f*. The lowest energy is found for Ti at the 8*i* site. The solution enthalpy for the 8*j* and 8*f* sites are by 20 and 29 meV/atom higher, respectively. This agrees with the Isnard neutron diffraction patterns [82], which revealed that Ti atoms are exclusively located at 8*i* sites. This strong 8*i* site preference of Ti atoms is mainly due to the larger Wigner-Seitz radius of the 8*i* site compared to 8*j* and 8*f* sites [93]. The 8*j* and 8*f* sites have similar energies, due to their similar local coordination [94].

Since we found the 8*i* site to be energetically favorable, we substituted the remaining Ti atoms only at this site and compared the energetics in Fig. 11. For a given Ti concentration, all possible configurations have been investigated and the energetically most favorable configuration is taken into account. Various different scenarios can be considered. Following the spirit of the plots in Figs. 5 and 8, we are in the first place interested in the phase formation energy of the ternary phases:

$$E^f(Ce_2Fe_{24-x}Ti_x) = E(Ce_2Fe_{24-x}Ti_x) - 2\mu_{Ce} - (24-x)\mu_{Fe} - x\mu_{Ti} \quad (9)$$

$$= 2E^f(CeFe_{12}) + E_0^{sol}(x) \quad (10)$$

The phases are thermodynamically stable, for negative formation energies. Although we still consider pure unaries as reference, we express the result in terms of the formation energy $E^f(CeFe_{12})$ of the unstable phase $CeFe_{12}$ (see Fig. 8). The correction is given by the Ti solution enthalpy in this phase, for which different formulations can be used. The natural reference are again the pure unaries:

$$E_0^{sol}(x) = E(Ce_2Fe_{24-x}Ti_x) - 2E(CeFe_{12}) + x(\mu_{Fe} - \mu_{Ti}). \quad (11)$$

As shown in Fig. 11 this expression yields a convex negative curve for the whole interval of *x*. Therefore, taking the small positive value of $E^f(CeFe_{12})$ in Eq. (10) into account, all *x* values result into compositions that are relevant for the discussion of phase stabilities.

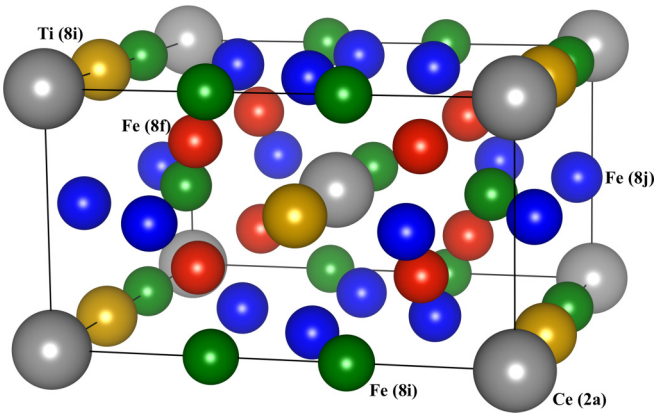

FIG. 12. Schematic representation of energetically most favorable crystal structure for the $CeFe_{11}Ti$.

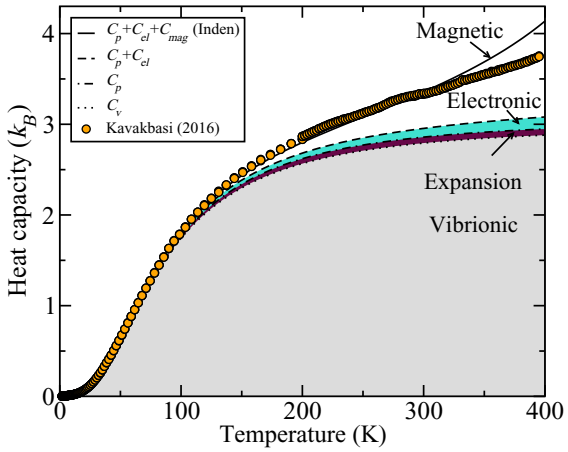

FIG. 13. Calculated heat capacity of $CeFe_{11}Ti$, separating the different free-energy contributions in Eq. (1). The results are compared with experimental results obtained by Kavakbasi [96].

However, there is a different scenario for the incorporation of Ti into the microstructure, namely by forming the B2-FeTi (or Fe_2Ti) phase. According to Fig. 5, there is a strong chemical driving force for this scenario, represented by the line $xE^f(\mathrm{FeTi})$ in Fig. 11. The effective solution enthalpy of Ti in $CeFe_{12}$ is therefore given with respect to the chemical potential of Ti in B2-FeTi (or Fe_2Ti) as

$$\begin{aligned} E_1^{\mathrm{sol}}(x) &= E(\mathrm{Ce_2Fe_{24-x}Ti_x}) - 2E(\mathrm{CeFe_{12}}) - xE(\mathrm{FeTi}) \\ &\quad + 2x\mu_{\mathrm{Fe}} \\ &= E_0^{\mathrm{sol}}(x) - xE^f(\mathrm{FeTi}). \end{aligned} \tag{12}$$

We note that the chemical potential of Ti in B2-FeTi and Fe_2Ti is almost the same at $T = 0$ K, due to straight line in the convex hull shown in Fig. 5. Using this definition, one can see in Fig. 11 that the substitution of two Ti atoms into the 26 atom supercell of $CeFe_{12}$ (7.7 at.% Ti) forms an energetic minimum of the system.

The consequence becomes even clearer, if we consider B2-FeTi (or Fe_2Ti) and a $1-12$ structure with lower Ti content as references:

$$\begin{aligned} E_2^{\mathrm{sol}}(x) &= E(\mathrm{Ce_2Fe_{24-x}Ti_x}) - E(\mathrm{Ce_2Fe_{24-x+1}Ti_{x-1}}) \\ &\quad - E(\mathrm{FeTi}) + 2\mu_{\mathrm{Fe}}. \end{aligned} \tag{13}$$

As shown in Fig. 11, the solution enthalpy of the third Ti atom is in this case slightly positive with a value of 40 meV/atom (60 meV/atom), indicating that a $1-12$ structure with two Ti atoms and the formation of B2-FeTi (or Fe_2Ti) is energetically more favorable.

Energetically favorable configurations for two Ti atoms in the supercell are obtained, when both substitutions are well separated. The configuration with the lowest energy is shown in Fig. 12, with a distance between the two Ti atoms of ∼5.20 Å. The configuration with the largest distance of ∼6.47 Å (bcc configuration) has almost the same energy, while a configuration of the two Ti atoms at nearest-neighbor 8*i* sites (distance ∼2.50 Å) is ∼0.7 eV higher in energy. This indicates a repulsive Ti-Ti interaction in the alloy.

Knowing the structure of $CeFe_{11}Ti$ we now turn over to the calculation of its physical and magnetic properties, shown in Table V. We observe a reasonable agreement between our theoretical results and available experimental data. For instance, the Fe atoms at the 8*i* site have the highest calculated magnetic moment, compared to the sites $8j$ and $8f$. This is a consequence of the larger Wigner-Seitz volume and smaller atomic coordination number and agrees with reported intrinsic magnetic properties of $RE(Fe_{11}Ti)$ alloys [95]. We further find that the substituted Ti atoms are aligned antiferromagnetically to the neighboring Fe atoms. This causes a suppression of the Fe magnetic moments, especially at the 8*i* site (compare to $CeFe_{12}$ in Table IV). The effect on the Ce sites seems, however, to be negligible.

We now concentrate on the finite-temperature properties of the identified $CeFe_{11}Ti$ structure. In Fig. 13, the computed heat capacity is compared with available experiments reported by Kavakbasi [96]. The experimental sample had the purity of 98.82 % of $CeFe_{11}Ti$, according to x-ray diffraction (XRD) analysis. Experiments were performed in a temperature range of 0–395 K. Again the agreement between the simulations and experimental measurements is found to be excellent up

TABLE V. Physical properties of stable $CeFe_{11}Ti$ compounds. The symbols are chosen as in Table II.

Alloy	a (Å)	c (Å)	B_0 (GPa)	M (μ_B)
$CeFe_{11}Ti$	8.524	4.680	132	2.30 Fe($8i$), 1.76 Fe($8f$), 2.18 Fe($8j$), −0.74 Ce($2a$), −1.07 Ti($8i$)
Exp.	8.539 [82]	4.780 [82]	-	17.4 [82][a], 15.0 [82][b], 19.19 [79][c]

[a]Experimental total magnetization (per f.u.) at 5 K. Our result is 20.95 μ_B/f.u. at 0 K.
[b]Experimental total magnetization (per f.u.) at 300 K.
[c]Theoretical total spin magnetization (per f.u.).

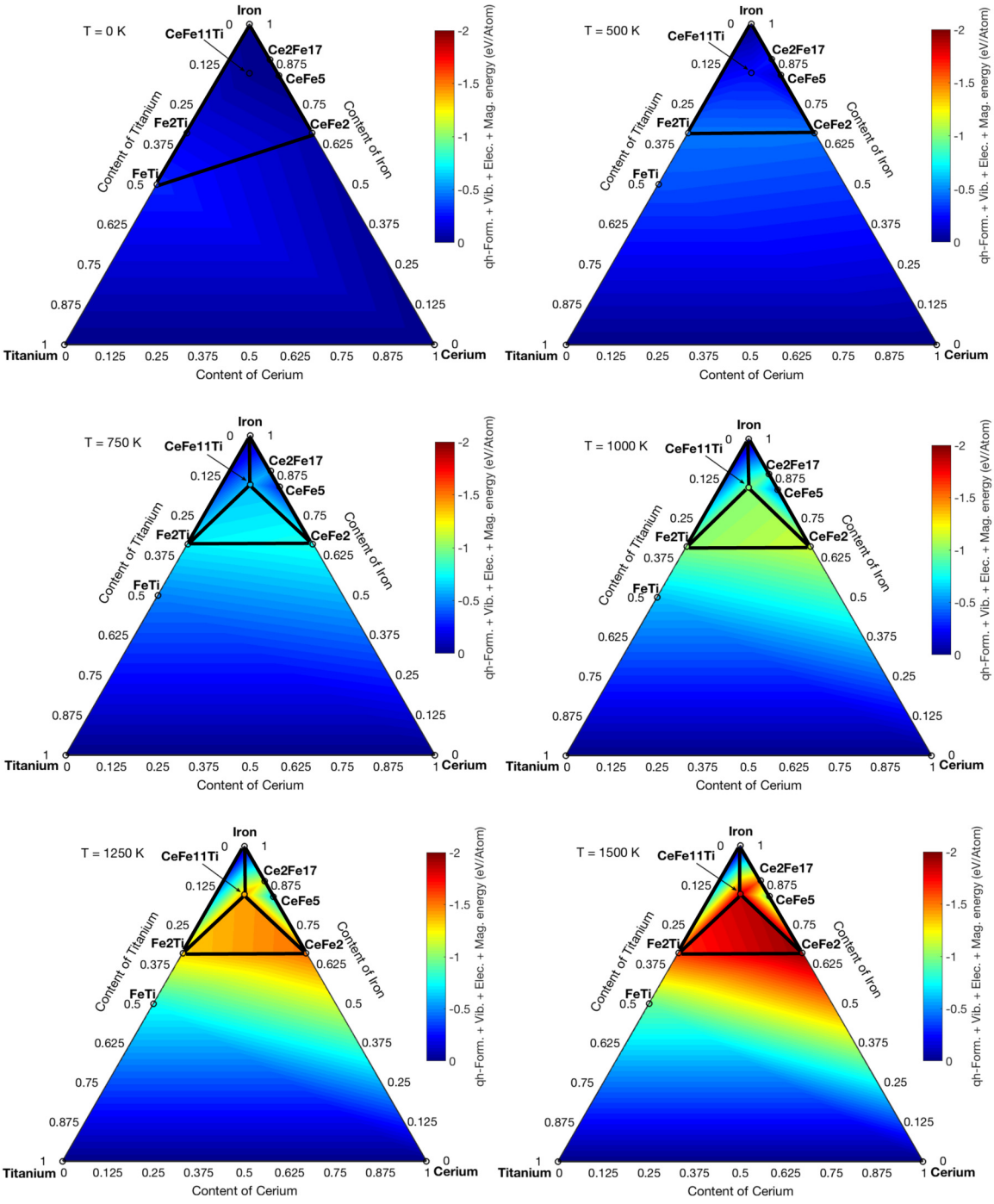

FIG. 14. Heat map of the calculated free energies of formation for the Ce-Fe-Ti phases that are indicated by black circles and labeled with their respective chemical compositions. Linear interpolation is used in between these data points, i.e., the colored area is similar to a convex hull between the structures with adjacent composition. The different diagrams correspond to 0, 500, 750, 1000, 1250, and 1500 K. The planes of the convex hull are highlighted by triangles (black lines) in the Fe-rich corner of the diagram (compare Fig. 2). Unary elements are taken as references, resulting into zero energy values for all temperatures. Furthermore, positive formation energies are set to zero.

to room temperature, further corroborating the reliability of our calculation scheme for free energies.

IV. FINITE-TEMPERATURE PHASE STABILITIES

In order to predict the phase stability of $CeFe_{11}Ti$, we have discussed in the previous section the incooperation of Ti into $CeFe_{12}$ in comparison with the formation of the B2-FeTi phase. Since the focus on Ti antisites and the choice of the compound with the lowest ground-state formation energy as a reference are unnecessary chemical and thermodynamic restrictions, we will now generalize this scheme. Already our experimental investigations in Fig. 1 indicate the relevance of the secondary phases Fe_2Ti and $CeFe_2$. In particular, the Laves

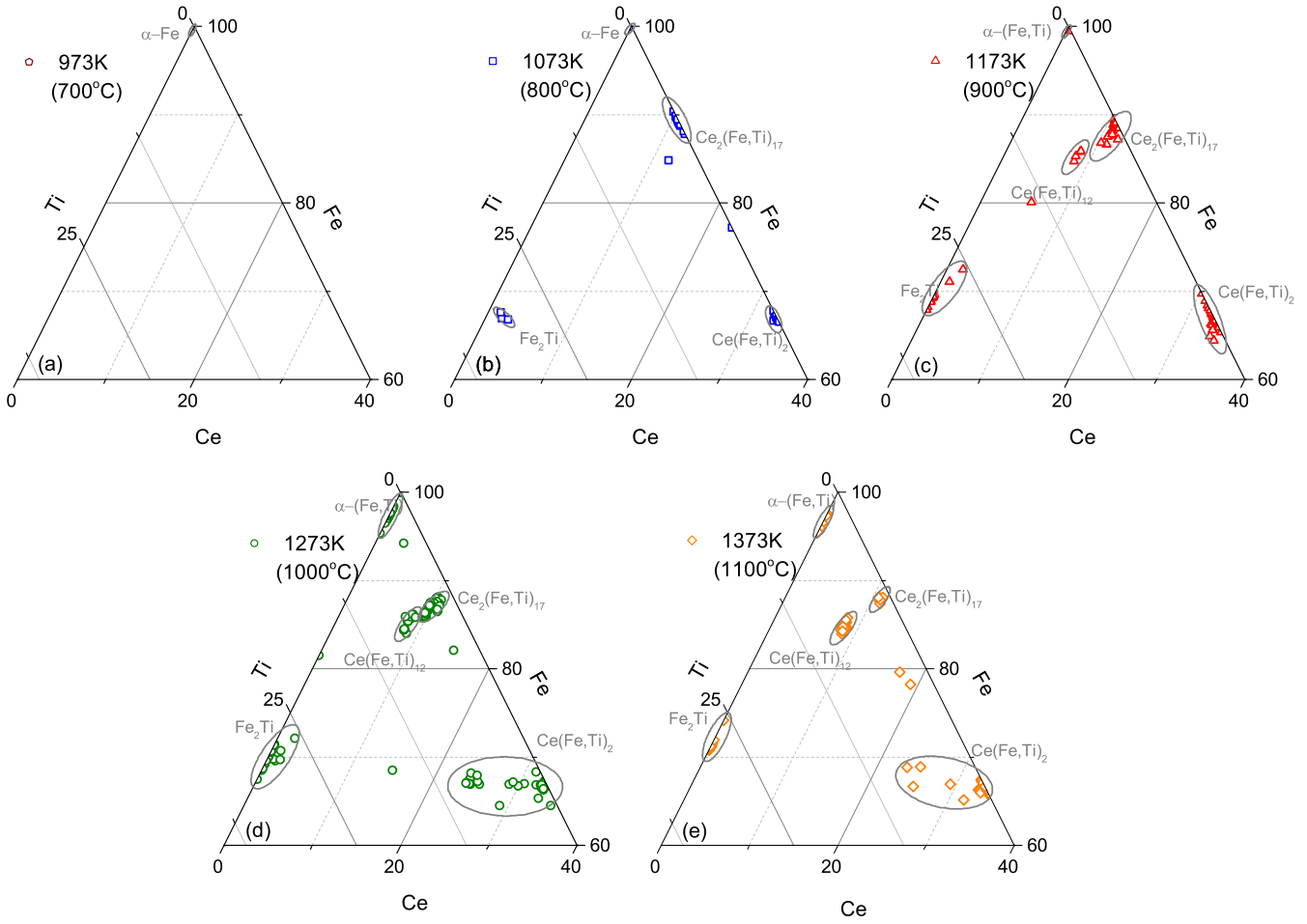

FIG. 15. Iron-rich regions of the phase diagrams of Ce-Fe-Ti system for the reactive crucibles prepared at (a) 700 °C, (b) 800 °C, (c) 900 °C, (d) 1000 °C, and (e) 1100 °C. Symbols indicate measured data points, while ellipses are guides to the eye.

phase $CeFe_2$ has been discussed in the literature as having a detrimental impact on magnetization and anisotropy [16,18]. Predicting the relative stability of these phases requires the consideration of the full composition space and the extension of the previous considerations to finite temperatures.

To this end, we use the representation of all relevant phases present in the ternary Ce-Fe-Ti system in terms of a Gibbs ternary diagram like in Fig. 2. Since we only consider stoichiometric line compounds, a standard isothermic phase diagram would not contain more information then the actual composition of the phases. Instead, we represent the formation energies of the binary systems Fe-Ti and Fe-Ce, as given at $T = 0$ K in Figs. 5 and 8, respectively, by a color code. In addition, the considerations in context of Fig. 11 lead to the conclusion that we can concentrate on $CeFe_{11}Ti$ as the most relevant ternary phase (though $Ce_2Fe_{23}Ti$ is another possibility). All other points inside the Gibbs triangle result from linear interpolations of the color code between these highlighted compositions. For low-energy structures, this corresponds to the convex hull, but the interpolation also connects structures that are above the common tangent between two or three other phases. In this way, also the formation energy of thermodynamically unstable phases is reflected by the coloring.

The result for $T = 0$ K as shown in the upper left diagram in Fig. 14 confirms that B2-FeTi, is the phase with the lowest ground-state formation energy. The energy of the phase with the second lowest formation energy, Fe_2Ti, corresponds to the linear interpolation between the energies of FeTi and pure Fe (compare Fig. 5). With increasing temperature, the energy of the Laves phase Fe_2Ti decreases well below this linear interpolation and becomes the lowest formation energy in the temperature window between ∼400 and 520 K. The main driving force for the stabilization of this phase is its magnetic entropy.

In the Ce-Fe system, the Ce_2Fe_{17} phase, which is unstable at 0 K, stabilizes with increasing temperature. This trend is much less significant for the $CeFe_5$ phase, which keeps a formation energy close to 0. The main reason of this stabilization is the relatively higher sub-lattice magnetization of the 2:17 phase. More important for our considerations is, however, that the total free energy of $CeFe_2$ becomes the lowest one for all temperatures above ∼520 K. Parallel to the binary phases, also the desired hard magnetic phase $CeFe_{11}Ti$ is stabilized with temperature as compared to the pure element reference systems, i.e., gets a negative formation energy. The formation energy becomes even lower than that of Fe_2Ti at a temperature of ∼1100 K. We observe very similar trends in our RCM studies ranging from 700 °C to 1100 °C,

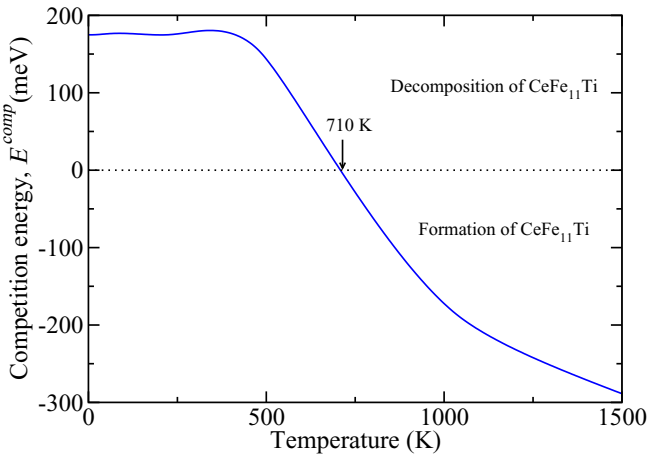

FIG. 16. Difference of the free energy of the hard-magnetic phase $CeFe_{11}Ti$ and the weighted sum of the free energies of α-Fe, Fe_2Ti, and $CeFe_2$, formed after a possible decomposition of $CeFe_{11}Ti$. The competition between phase formation and decomposition determines the critical temperature for the phase stability of $CeFe_{11}Ti$.

which are also displayed in terms of Gibbs ternary diagrams (Fig. 15): (i) In agreement with our theoretical prediction, the Laves phases Fe_2Ti and $CeFe_2$ only emerge at elevated temperatures and become increasingly important with raising temperature. Nevertheless, the critical temperature seems to be higher in experiment ($\sim$1000 K) than in theory ($\sim$500 K). This might be connected to the fact that also the B2-FeTi phase is not seen in the experimental crucibles processed below 1073 K, while theory predicts its presence down to the ground state, see Fig. 5. On the other hand, experiments resolve a Ti solubility in α-Fe at elevated temperatures that has been ignored in theory. (ii) The second common feature is the occurrence of the Ce_2Fe_{17} phase, rather than the $CeFe_5$ phase in the binary Fe-Ce system, though there is again a different critical temperature. Experimental indications for a solubility of Ti in this phase have also not been addressed theoretically. (iii) Most important is, however, the agreement in the prediction of a critical temperature for the presence of the $CeFe_{11}Ti$. The noticeable solubility range of Ti and the restriction to Ti concentrations below 10 at.% are also in good agreement with the theoretical investigations in context of Fig. 11.

In the following, we aim at a determination of the critical temperature for the stability $CeFe_{11}Ti$ within our *ab initio* approach. To this end, we note already a temperature trend for the relative formation energies in Fig. 14: up to 750 K the Laves phases Fe_2Ti and $CeFe_2$ seem to be dominant, suggesting a phase decomposition into pure Fe, Fe_2Ti and $CeFe_2$ for samples with a nominal composition in the upper triangle of Fig. 2. At 1000 and 1250 K, however, a triangle formed by $CeFe_{11}Ti$, Fe_2Ti and $CeFe_2$ dominates the phase formation diagram, in favor of the relative phase stability of $CeFe_{11}Ti$.

For a more quantitative evaluation of this transition, we need to determine the free energy of the phase $CeFe_{11}Ti$ relative to a possible decomposition into the phases α-Fe, Fe_2Ti and $CeFe_2$, as highlighted by the blue lines in Fig. 2. This competition is expressed by the energy difference

$$F^{\mathrm{comp}} = F(\mathrm{CeFe_{11}Ti}) - (F(\mathrm{CeFe_2}) + F(\mathrm{Fe_2Ti}) + 7F(\mathrm{Fe})). \tag{14}$$

Here, a positive (negative) value of F^{comp} means that the decomposition of $CeFe_{11}Ti$ into the corresponding phases is (is not) favored.

The expression generalizes the competition for the Ti incorporation in $CeFe_{12}$ versus B2-FeTi discussed above. First, it now handles all three alloying elements on equal footing. The large weighting factor in front of F(Fe) reflects the fact that we are in the Fe-rich corner of the phase diagram and is chosen to ensure stoichiometry. Second, it considers the Laves phases Fe_2Ti and $CeFe_2$ as reference systems for Ti and Ce, respectively, since we have proven that they become most stable at elevated temperatures. This is further confirmed by our experimental results in Figs. 1 and 15. Third, it is formulated for free energies at finite temperatures, including the $F^{el} + F^{vib} + F^{mag}$ entropy terms.

Figure 16 visualizes this temperature dependence of the competition energy. It is seen that $CeFe_{11}Ti$ will be thermodynamically stable above 710 K. Below this temperature, the promising ternary phase can decompose into the considered competing phases, including in particular the detrimental phase $CeFe_2$. There is a driving force of 175 meV/f.u. on $CeFe_{11}Ti$ to decompose at 0 K. The competition energy has two shallow maximums at low temperatures, which are due to the Curie temperatures of $CeFe_2$ (228 K), Fe_2Ti (280 K), and $CeFe_{11}Ti$ (485 K). This observation is decisive for the design and sustainability of the promising hard magnetic phase $CeFe_{11}Ti$. Strategies to improve this thermodynamic stability, i.e., by chemical alloying, need to reduce this critical temperature.

V. DISCUSSION AND CONCLUSION

In conclusion, starting from unary Ce, a large set of binary and ternary intermetallics in the Ce-Fe-Ti system are systematically studied at $T = 0$ K as well as at finite temperatures. We applied the quasiharmonic approximation to access finite temperature phase stabilities. Experimentally available phonon dispersions and heat capacities are compared with the calculated data in order to assess the quality of the derived free energies. Our free energy calculations reveal the stability of the $CeFe_2$ phase, which is detrimental for the design of hard-magnetic materials. Furthermore, we observe the formation of the Ce_2Fe_{17} phase, while $CeFe_5$ will not play a role in the phase diagram. Most importantly, however, we predict that the hard magnetic phase of the $ThMn_{12}$-type $Ce(Fe, Ti)_{12}$ will only be stable if the Ti content is approximately equal to the Ce content and the annealing temperature is above 700 K.

The predictions are in overall perfect agreement with experimental phase diagrams obtained from the high-throughput synthesis method [reactive crucible melting (RCM)]. In this case the $ThMn_{12}$-type $Ce(Fe, Ti)_{12}$ phase contains almost the same Ti content and the stabilization temperature is slightly higher than in theory ($\approx$1000 K). The RCM yields additional information about solubility ranges in the different phases, like the onset of Ti solubility in the phase $Ce_2(Fe, Ti)_{17}$ above

1073 K, which will be a topic of upcoming investigations within the *ab initio* approach.

ACKNOWLEDGMENTS

Our project on rare-earth based alloys for hard-magnetic applications: temperature and pressure dependent phase stabilities (RE-MAP) is supported by Deutsche Forschungsgemeinschaft (DFG Project No. 316912154) and Agence nationale de la recherche (ANR, Grant No. ANR-16-CE92-0029). The partial finance by Bosch-Forschungsstiftung for this work is acknowledged. We are also grateful to Thomas Eckl and Holger Wüst for fruitful discussions and experimental supports for Gerhard Wilde, Bengü Tas Kavakbasi, and Monika Nellessen.

[1] O. Gutfleisch, M. Willard, E. Brück, C. H. Chen, S. G. Sankar, and J. P. Liu, Magnetic materials and devices for the 21st century: Stronger, lighter, and more energy efficient, Adv. Mater. **23**, 821 (2011).

[2] J. J. Croat, J. F. Herbst, R. W. Lee, and F. E. Pinkerton, Pr-Fe and Nd-Fe-based materials: A new class of high-performance permanent magnets (invited), J. Appl. Phys. **55**, 2078 (1984).

[3] M. Sagawa, S. Fujimura, N. Togawa, H. Yamamoto, and Y. Matsuura, New material for permanent magnets on a base of Nd and Fe (invited), J. Appl. Phys. **55**, 2083 (1984).

[4] M. Sagawa, S. Fujimura, H. Yamamoto, Y. Matsuura, and K. Higara, Permanent magnet materials based on the rare earth-iron-boron tetragonal compounds (invited), IEEE Trans. Magn. **20**, 1584 (1984).

[5] L. Li, J. Yi, Y. Peng, and B. Huang, The effect of compound addition Dy_2O_3 and Sn on the structure and properties of NdFeNbB magnets, J. Magn. Magn. Mater. **308**, 80 (2007).

[6] D. Bauer, D. Diamond, J. Li, D. Sandalow, P. Telleen, and B. Wanner, Critical Materials Strategy, US Department of Energy Office of Policy and International Affairs (PI) (2011), https://www.energy.gov/sites/prod/files/DOE_CMS2011_FINAL_Full.pdf.

[7] M. Pellegrini, Report on Critical Raw Materials for the Eu, report of the ad hoc working group on defining critical raw materials, European Commission, DG Enterprise and Industry, (2014), http://ec.europa.eu/DocsRoom/documents/10010/attachments/1/translations/en/renditions/native.

[8] K. P. Skokov and O. Gutfleisch, Heavy rare earth free, free rare earth and rare earth free magnets - Vision and reality, Scr. Mater. **154**, 289 (2018).

[9] I. Poenaru, A. Lixandru, S. Riegg, B. Fayyazi, A. Taubel, K. Güth, R. Gauß, and O. Gutfleisch, Ce and La as substitutes for Nd in $Nd_2Fe_{14}B$-based melt-spun alloys and hot-deformed magnets: A comparison of structural and magnetic properties, J. Magn. Magn. Mater. **478**, 198 (2019).

[10] G. Tyler, Rare earth elements in soil and plant systems - A review, Plant Soil **267**, 191 (2004).

[11] S. Massari and M. Ruberti, Rare earth elements as critical raw materials: Focus on international markets and future strategies, Resources Policy **38**, 36 (2013).

[12] R. J. Radwanski, The Rare Earth Contribution to the Magnetocrystalline Anisotropy in RCo_5 Intermetallics, J. Magn. Magn. Mater. **62**, 120 (1986).

[13] D. Fruchart, F. Vaillant, A. Yaouanc, J. M. D. Coey, R. Fruchart, P. L'heritier, T. Riesterer, J. Osterwalder, and L. Schlapbach, Hydrogen induced changes of valency and hybridization in Ce intermetallic compounds, J. Less-Common Met. **130**, 97 (1987); L. Vinet and A. Zhedanov, A 'missing' family of classical orthogonal polynomials, J. Phys. A: Math. Theor. **44**, 085201 (2011).

[14] T. W. Capehart, R. K. Mishra, G. P. Meisner, C. D. Fuerst, and J. F. Herbst, Steric variation of the cerium valence in $Ce_2Fe_{14}B$ and related compounds, Appl. Phys. Lett. **63**, 3642 (1993).

[15] J. F. Herbst, M. S. Meyer, and F. E. Pinkerton, Magnetic hardening of $Ce_2Fe_{14}B$, J. Appl. Phys. **111**, 07A718 (2012).

[16] M. Xing, J. Han, Z. Lin, F. Wan, C. Li, S. Liu, C. Wang, J. Yang, and Y. Yang, Anisotropic ternary $Ce_{13}Fe_{80}B_7$ powders prepared by hydrogenation-disproportionation-desorption-recombination process and the diffusion of Ce-Cu eutectic alloys, J. Magn. Magn. Mater. **331**, 140 (2013).

[17] E Niu, Z. A. Chen, G. A. Chen, Y. G. Zhao, J. Zhang, X. L. Rao, B. P. Hu, and Z. X. Wang, Achievement of high coercivity in sintered R-Fe-B magnets based on misch-metal by dual alloy method, J. Appl. Phys. **115**, 113912 (2014).

[18] M. Zhang, Y. Liu, Z. Li, L. Peng, B. Shen, and F. Hu, Magnetization process of nanocrystalline mischmetal-Fe-B ribbons, J. Alloys Compd. **688**, 1053 (2016).

[19] C. Yan, S. Guo, R. Chen, D. Lee, and A. Yan, Enhanced magnetic properties of sintered Ce-Fe-B-based magnets by optimizing the microstructure of strip-casting alloys, IEEE Trans. Magn. **50**, 2104604 (2014).

[20] Z. Chen, Y. K. Lim, and D. Brown, Substitution of Ce for (Nd,Pr) in melt-spun (Nd,Pr)-Fe-B powders, IEEE Trans. Magn. **51**, 2102104 (2015).

[21] Q. Y. Zhou, Z. Liu, S. Guo, A. R. Yan, and D. Lee, Magnetic properties and microstructure of melt-spun Ce-Fe-B magnets, IEEE Trans. Magn. **51**, 2104304 (2015).

[22] C. J. Yan, S. Guo, R. J. Chen, D. Lee, and A. R. Yan, Phase constitution and microstructure of Ce–Fe–B strip-casting alloy, Chin. Phys. B **23**, 107501 (2014).

[23] X. Chen, Y. G. Chen, Y. B. Tang, and D. Q. Xiao, 1:13 phase formation mechanism and first-order magnetic transition strengthening characteristics in $(La,Ce)Fe_{13-x}Si_x$ alloys, Rare Metals **35**, 691 (2016).

[24] M. Zhang, Z. Li, B. Shen, F. Hu, and J. Sun, Permanent magnetic properties of rapidly quenched $(La, Ce)_2Fe_{14}B$ nanomaterials based on La-Ce mischmetal, J. Alloys Compd. **651**, 144 (2015).

[25] G. Kresse and J. Furthmüller, Efficient iterative schemes for *ab initio* total-energy calculations using a plane-wave basis set, Phys. Rev. B **54**, 11169 (1996).

[26] P. E. Blöchl, Projector augmented-wave methods, Phys. Rev. B **50**, 17953 (1994).

[27] J. P. Perdew, K. Burke, and M. Ernzerhof, Generalized Gradient Approximation Made Simple, Phys. Rev. Lett. **77**, 3865 (1996).

[28] D. C. Koskimaki, K. A. Gschneidner, and N. T. Panousis, Preparation of single phase β and α cerium samples for low temperature measurements, J. Cryst. Growth **22**, 225 (1974).

[29] S. L. Dudarev, G. A. Botton, S. Y. Savrasov, C. J. Humphreys, and A. P. Sutton, Electron-energy-loss spectra and the structural stability of nickel oxide: An LSDA + U study, Phys. Rev. B **57**, 1505 (1998).

[30] T. Hickel, B. Grabowski, F. Körmann, and J. Neugebauer, Advancing density functional theory to finite temperatures: Methods and applications in steel design, J. Phys.: Condens. Matter **24**, 053202 (2012).

[31] N. D. Mermin, Thermal properties of the inhomogeneous electron gas, Phys. Rev. **137**, A1441 (1965).

[32] X. Zhang, B. Grabowski, F. Körmann, C. Freysoldt, and J. Neugebauer, Accurate electronic free energies of the 3*d*, 4*d*, and 5*d* transition metals at high temperatures, Phys. Rev. B **95**, 165126 (2017).

[33] K. Parlinski, Z. Q. Li, and Y. Kawazoe, First-Principles Determination of the Soft Mode in Cubic ZrO_2, Phys. Rev. Lett. **78**, 4063 (1997).

[34] B. Grabowski, T. Hickel, and J. Neugebauer, *Ab initio* study of the thermodynamic properties of nonmagnetic elementary fcc metals: Exchange-correlation-related error bars and chemical trends, Phys. Rev. B **76**, 024309 (2007).

[35] D. C. Wallace, *Thermodynamics of Crystals* (Dover, New York, 1998).

[36] L. Zhou, F. Körmann, D. Holec, M. Bartosik, B. Grabowski, J. Neugebauer, and P. H. Mayrhofer, Structural stability and thermodynamics of CrN magnetic phases from *ab initio* calculations and experiment, Phys. Rev. B **90**, 184102 (2014).

[37] F. Körmann, A. Al Hasan Breidi, S. L. Dudarev, N. Dupin, G. Ghosh, T. Hickel, P. Korzhavyi, J. A. Muñoz, and I. Ohnuma, Lambda transitions in materials science: Recent advances in CALPHAD and first-principles modelling, Phys. Status Solidi B **251**, 53 (2014).

[38] G. Inden, in *Proceedings of CALPHAD V* (Max-Planck-Institut für Eisenforschung, Dsseldorf, Germany, 1976), pp. 1–13.

[39] M. Hillert and M. Jarl, A model for alloying effects ferromagnetic metals, Calphad **2**, 227 (1978).

[40] Q. Chen and B. Sundman, Modeling of thermodynamic properties for Bcc, Fcc, liquid, and amorphous iron, J. Phase Equilib. **22**, 631 (2001).

[41] W. Xiong, Q. Chen, P. A. Korzhavyi, and M. Selleby, An improved magnetic model for thermodynamic modeling, Calphad: Computer Coupling of Phase Diagrams and Thermochemistry **39**, 11 (2012).

[42] H. Sawada, K. Kawakami, F. Koermann, B. Grabowski, T. Hickel, and J. Neugebauer, Acta Materialia Partitioning of Cr and Si between cementite and ferrite derived from first-principles thermodynamics, Acta Mater. **102**, 241 (2016).

[43] F. Gross, Search for new permanent magnetic phases by the reaction crucible analysis and development of new high through put methods, Ph.D. thesis, University of Birmingham, 2004.

[44] D. Goll, R. Loeffler, J. Herbst, R. Karimi, and G. Schneider, High-throughput search for new permanent magnet materials, J. Phys.: Condens. Matter **26**, 064208 (2014).

[45] S. Ener, J. Kroder, K. P. Skokov, and O. Gutfleisch, The search for room temperature tetragonal phases of Fe-Mn-Ga: A reactive crucible melting approach, J. Alloys Compd. **683**, 198 (2016).

[46] B. Fayyazi, K. P. Skokov, T. Faske, D. Y. Karpenkov, W. Donner, and O. Gutfleisch, Bulk combinatorial analysis for searching new rare-earth free permanent magnets: Reactive crucible melting applied to the Fe-Sn binary system, Acta Mater. **141**, 434 (2017).

[47] P. Villars, *Pearson's Handbook Crystallographic Data for Intermetallic Phases*, Desk edition (ASM International, Materials Park, Ohio, 1997), Vol. 1, pp. 1161–1166.

[48] J. S. Olsen, L. Gerward, U. Benedict, and J. P. Itié, The crystal structure and the equation of state of cerium metal in the pressure range 0-46 Gpa, Physica B+C **133**, 129 (1985).

[49] D. Glötzel, Ground-state properties of f band metals: Lanthanum, cerium and thorium, J. Phys. F **8**, L163 (1978).

[50] W. H. Zachariasen and F. H. Ellinger, The crystal structures of cerium metal at high pressure, Acta Crystallogr. Sect. A **A33**, 155 (1977).

[51] D. C. Koskimaki and K. A. Gschneidner, Heat capacity and magnetic susceptibility of single-phase α-cerium, Phys. Rev. B **11**, 4463 (1975).

[52] M. R. MacPherson, G. E. Everett, D. Wohlleben, and M. B. Maple, Magnetic Susceptibility of Cerium Metal Under Pressure, Phys. Rev. Lett. **26**, 20 (1971).

[53] C. Kittel, *Introduction to Solid State Physics*, 6th ed. (Wiley, New York, 1986).

[54] S. Allard, *Metals, Thermal and Mechanical Data: International Tables of Selected Constants* (Pergamon, Oxford, 1969), Vol. 16.

[55] J. Neugebauer and T. Hickel, Density functional theory in materials science, Wiley Interdiscip. Rev.: Comp. Mol. Sci. **3**, 438 (2013).

[56] W. E Pickett, A. J. Freeman, and D. D. Koelling, Local-density-functional approach to the isostructual $\gamma - \alpha$ transition in cerium using the self-consistent linearized-augmented-plane-wave method, Phys. Rev. B **23**, 1266 (1981).

[57] P. Söderlind, O. Eriksson, J. Trygg, B. Johansson, and J. M. Wills, Density-functional calculations for cerium metal, Phys. Rev. B **51**, 4618 (1995).

[58] A. Svane, Electronic structure of cerium in the self-interaction-corrected local-spin-density approximation, Phys. Rev. B **53**, 4275 (1996).

[59] T. Jarlborg, E. G. Moroni, and G. Grimvall, α-γ transition in Ce from temperature-dependent band-structure calculations, Phys. Rev. B **55**, 1288 (1997).

[60] F. Tran, F. Karsai, and P. Blaha, Nonmagnetic and ferromagnetic fcc cerium studied with one-electron methods, Phys. Rev. B **89**, 155106 (2014).

[61] B. Amadon, S. Biermann, A. Georges, and F. Aryasetiawan, The α-γ Tansition of Cerium is Entropy Driven, Phys. Rev. Lett. **96**, 066402 (2006).

[62] D. M. Wieliczka, C. G. Olson, and D. W. Lynch, High-resolution photoemission study of γ- and α-cerium, Phys. Rev. B **29**, 3028 (1984).

[63] E. Weschke, C. Laubschat, T. Simmons, M. Domke, O. Strebel, and G. Kaindl, Surface and bulk electronic structure of Ce metal studied by high-resolution resonant photoemission, Phys. Rev. B **44**, 8304 (1991).

[64] C. Stassis, T. Gould, O. D. McMasters, K. A. Gschneidner, Jr., and R. M. Nicklow, Lattice and spin dynamics of γ Ce, Phys. Rev. B **19**, 5746 (1979).

[65] J. L. Murray, The Fe-Ti (Iron-Titanium) system, Bull. Alloy Phase Diagrams **2**, 320 (1981).

[66] P. J. Brown, J. Deportes, and B. Ouladdiaf, Magnetic structure of the Laves phase compound $TiFe_2$, J. Phys.: Condens. Matter **4**, 10015 (1992).

[67] U. Buchenau, H. R. Schober, J. M. Welter, G. Arnold, and R. Wagner, Lattice dynamics of $Fe_{0.5}Ti_{0.5}$, Phys. Rev. B **27**, 955 (1983).

[68] J. Y. Rhee, B. N. Harmon, and D. W. Lynch, Optical properties and electronic structures of equiatomic XTi(X = Fe, Co, and Ni) alloys, Phys. Rev. B **54**, 17385 (1996).

[69] J. Liebertz, S. Stähr, and S. Haussühl, Growth and properties of single crystals of FeTi, Kristall und Technik **15**, 1257 (1980).

[70] C. G. Schön, A. V. Gil Rebaza, V. I. Fernández, L. T. F. Eleno, P. G. Gonzales-Ormeño, L. A. Errico, and H. M. Petrilli, Magnetism and stability interplay: Correlations in simple BCC-based Fe intermetallic compounds, J. Alloys Compd. **688**, 337 (2016).

[71] Y. Wu, X. Wu, S. Qin, and K. Yang, Compressibility and phase transition of intermetallic compound Fe_2Ti, J. Alloys Compd. **558**, 160 (2013).

[72] L.-F. Zhu, M. Friák, A. Udyansky, D. Ma, A. Schlieter, U. Kühn, J. Eckert, and J. Neugebauer, *Ab initio* based study of finite-temperature structural, elastic and thermodynamic properties of FeTi, Intermetallics **45**, 11 (2014).

[73] K. H. J. Buschow and J. S. van Wieringen, Crystal structure and magnetic properties of cerium-iron compounds, Phys. Status Solidi B **42**, 231 (1970).

[74] Y. C. Chuang, C. H. Wu, and Z. B. Shao, Investigation of the Ce-Fe binary system, J. Less-Common Met. **136**, 147 (1987).

[75] H. Okamoto, Ce-Fe (Cerium-Iron), J. Phase Equilib. Diffus. **29**, 116 (2008).

[76] D. Braithwaite, G. Lapertot, B. Salce, A.-M. Cumberlidge, and P. L. Alireza, Antiferromagnetic order in pure $CeFe_2$ under pressure, Phys. Rev. B **76**, 224427 (2007).

[77] R. Das and S. K. Srivastava, in *Proceedings Of the International Conference on Condensed Matter Physics 2014 (ICCMP 2014)*, edited by R. Sharma, P. K. Ahluwalia, and M. Singh, AIP Conf. Proc. No. 1661 (AIP, New York, 2015).

[78] J. O. Jepson and P. E. Duwez, Partial Phase Diagram of the Iron Cerium Diagram, Trans. Am. Soc. Met. **47**, 543 (1955).

[79] L. Ke and D. D. Johnson, Intrinsicmagnetic properties in $R(Fe_{1-x}Co_x)_{11}TiZ$(R = Y and Ce; Z = H, C, and N), Phys. Rev. B **94**, 024423 (2016).

[80] W. Körner, G. Krugel, and C. Elsässer, Theoretical screening of intermetallic $ThMn_{12}$-type phases for new hard-magnetic compounds with low rare earth content, Sci. Rep. **6**, 24686 (2016).

[81] Y. Makihara, Y. Uwatoko, H. Matsuoka, M. Kosaka, H. Fukuda, and H. Fujii, Magnetism in single crystal Ce_2Fe_{17} with two types of magnetic ground states, J. Magn. Magn. Mater. **272-276**, 551 (2004).

[82] O. Isnard, S. Miraglia, M. Guillot, and D. Fruchart, Hydrogen effects on the magnetic properties of $RFe_{11}Ti$ compounds, J. Alloys Compd. **275-277**, 637 (1998).

[83] F. R. De Boer, Y. K. Huang, D. B. De Mooij, and K. H. J. Buschow, Magnetic properties of a series of novel ternary intermetallics ($RFe_{10}V_2$), J. Less-Common Met. **135**, 199 (1987).

[84] C. Zhou and F. E. Pinkerton, Magnetic hardening of $CeFe_{12-x}Mo_x$ and the effect of nitrogenation, J. Alloys Compd. **583**, 345 (2014).

[85] C. Zhou, F. E. Pinkerton, and J. F. Herbst, Formation of $TbCu_7$-type $CeFe_{10}Zr_0.8$ by rapid solidification, J. Alloys Compd. **569**, 6 (2013).

[86] C. Zhou, F. E. Pinkerton, and J. F. Herbst, High Curie temperature of Ce-Fe-Si compounds with $ThMn_{12}$ structure, Scr. Mater. **95**, 66 (2015).

[87] L. Paolasini, B. Hennion, A. Panchula, K. Myers, and P. Canfield, Lattice dynamics of cubic Laves phase ferromagnets, Phys. Rev. B **58**, 12125 (1998).

[88] A. Haldar, K. G. Suresh, and A. K. Nigam, Magnetic and magnetocaloric properties of $Ce_{1-x}R_xFe_2$ and $Ce(Fe_{1-x}M_x)_2$ compounds, J. Phys. D **43**, 285004 (2010).

[89] F. Körmann, A. Dick, B. Grabowski, B. Hallstedt, T. Hickel, and J. Neugebauer, Free energy of bcc iron: Integrated *ab initio* derivation of vibrational, electronic, and magnetic contributions, Phys. Rev. B **78**, 033102 (2008).

[90] G. Inden, The role of magnetism in the calculation of phase diagrams, Physica B+C **103**, 82 (1981).

[91] N. Drebov, A. Martinez-Limia, L. Kunz, A. Gola, T. Shigematsu, T. Eckl, P. Gumbsch, and C. Elsässer, *Ab initio* screening methodology applied to the search for new permanent magnetic materials, New J. Phys. **15**, 125023 (2013).

[92] B.-P. Hu, H.-S. Li, and J. M. D. Coey, Relationship between $ThMn_{12}$ and Th_2Ni_{17} structure types in the $YFe_{11-x}Ti_x$ alloy series, J. Appl. Phys. **67**, 4838 (1990).

[93] O. Isnard, Role of interstitial elements on permanent magnet alloys based on rare earth elements and iron: Synthesis, structural study, spectroscopic analysis in relation to magnetic properties, Ph.D. thesis, University Grenoble, 1993.

[94] Y. Wang, J. Shen, N. X. Chen, and J. L. Wang, Theoretical investigation on site preference of foreign atoms in rare-earth intermetallics, J. Alloys Compd. **319**, 62 (2001).

[95] B.-P. Hu, H.-S. Li, J. P. Gavigan, and J. M. D. Coey, Intrinsic magnetic properties of the iron-rich $ThMn_{12}$-structure alloys $R(Fe_{11}Ti)$; R = Y, Nd, Sm, Gd, Tb, Dy, Ho, Er, Tm and Lu, J. Phys.: Condens. Matter **1**, 755 (1989).

[96] B. T. Kavakbasi, Heat capacity measurement (unpublished).